

PAPER • OPEN ACCESS

## Thermographic phosphor heat flux measurements of laminar methane/air flame impinging on a cylindrical surface

To cite this article: Peter Obara Oketch *et al* 2019 *Meas. Sci. Technol.* **30** 094003

View the [article online](#) for updates and enhancements.

You may also like

- [Gas compositional and pressure effects on thermographic phosphor thermometry](#)  
J Brübach, A Dreizler and J Janicka
- [Effects of coaxial airflow swirl number on combustion and flame characteristics of methane/air and n-butane/air flames in a miniature-scale swirl burner](#)  
Soroush Sheykhbaglou and Seyed Mostafa Robati
- [Development of an automatic routine for calibration of thermographic phosphors](#)  
F Abou Nada, C Knappe, X Xu et al.

# Thermographic phosphor heat flux measurements of laminar methane/air flame impinging on a cylindrical surface

Peter Obara Oketch<sup>✉</sup>, Munko Gonchikzhapov, Ulf Bergmann and Burak Atakan

Thermodynamic, IVG, Faculty of Engineering, University of Duisburg-Essen, Lotharstr. 1, D-47057, Germany

E-mail: [peter.oketch@stud.uni-due.de](mailto:peter.oketch@stud.uni-due.de)

Received 30 November 2018, revised 11 April 2019

Accepted for publication 13 May 2019

Published 26 July 2019



## Abstract

The stagnation point heat fluxes of methane/air flames impinging normal on a cylindrical surface were determined experimentally. Light induced phosphorescence from thermographic phosphors was used to investigate surface temperatures at the stagnation point from a nearly 1D laminar premixed flame burning against a water-cooled ceramic tube. The ceramic tube was coated with 1.1% chromium-doped alumina (ruby) at the impingement area and excited with a green light-emitting diode (LED) to measure the surface temperature. The flame temperature profiles were also measured with a thermocouple of type R (Pt/Pt + 13% Rh). Effects on variations in cold gas velocity ( $0.1 \text{ m s}^{-1}$ – $0.5 \text{ m s}^{-1}$ ) relative to the flame speed, equivalence ratio ( $\Phi = 0.85$ – $1.2$ ), burner to impingement surface spacing ( $H/d = 0.5$ – $2$ ) and surface curvature are reported. The stagnation point heat fluxes are strongly influenced by the flame stabilization mechanism, which changes from burner to wall stabilization, which also is seen from the measured flame temperature profiles. Increasing the cold gas velocity of the reactants leads to higher stagnation point heat fluxes. In addition, decreasing the distance between the burner and impingement surface increases the heat flux, with higher heat fluxes recorded for a tube compared to a flat plate.

Keywords: thermographic phosphors, light induced phosphorescence, flame impingement, thermocouple, heat flux

(Some figures may appear in colour only in the online journal)

## 1. Introduction

Flame jet impingement heating has been investigated over past decades because of its high heat flux rates compared to other convective heat transfer schemes. Due to the direct impingement of the flame on the target surface, the convective heat transfer coefficients are high in such processes. For a single round flame jet, impinging on a flat surface, which commonly serves as the fundamental configuration amongst

others, scientific work is well documented [1–4]. On the other hand, the number of published articles on flame jet impingement on curved surfaces is limited. This configuration is encountered in different industrial processes, such as heating and melting of metals and glass [5]. Here, the flow fields in axial and angular directions differ between curved and flat surfaces, resulting in different heat transfer characteristics [6]. Most of the investigated cases of laminar flame jet impingement on curved surfaces, have reported the heat transfer from such jets in terms of the Nusselt number as a function of Reynolds number or a dimensionless distance. Few studies have considered the probably more important characteristic number: the cold gas velocity of the reactants exiting from the



Original content from this work may be used under the terms of the [Creative Commons Attribution 3.0 licence](https://creativecommons.org/licenses/by/3.0/). Any further distribution of this work must maintain attribution to the author(s) and the title of the work, journal citation and DOI.

burner relative to the laminar flame velocity, which in turn is related to the Nusselt number. Salem *et al* [7] investigated this parameter but only for methane/air flame impinging on a flat surface and reported the change of heat transfer characteristics with the change of flame stabilization mechanism from burner stabilization to plate stabilization.

Chander and Ray [6] studied experimentally the heat transfer characteristics of laminar methane/air flames impinging normally on a cylindrical surface. Effects of Reynolds number, equivalence ratio, separation distance and burner diameter to cylinder diameter ratio were investigated. Higher stagnation point heat fluxes were reported for the cylindrical surfaces compared to the flat surfaces. In addition, the stagnation point heat flux increased as the surface curvature ( $d/D$ ) was reduced. The surface curvature was taken as the ratio of the burner diameter ( $d$ ) to the cylinder diameter ( $D$ ). They developed correlations for the stagnation point Nusselt number, but the calculations were made with the adiabatic flame temperature as the reference temperature, instead of the gas phase temperature outside the thermal boundary layer. This definition may get problematic, if the amount of heat transfer to the burner gets important, as in burner-stabilized flames; the temperature, and thus the heat flux, will then also depend on the burner details. The heat fluxes in these experimental study were obtained by measurements with heat flux micro-sensors [1, 6]. Micro-sensors are easy to use but are inherently intrusive and their presence on the surface can result in boundary layer growth. This is common for smaller cylindrical surfaces when the cylinder dimensions are comparable to that of the micro-sensor, which may result in insufficient resolution. Therefore, a necessity for other techniques with high accuracy and precision for the heat fluxes determination on different surface geometries from flame jet impingement. Depending on the method employed, the temperatures across the solid walls or the gas phase temperatures of the flame near the impingement surface can be measured for the evaluation of wall heat transfer.

For the wall surface temperature measurements, different well-established techniques such as thermocouples, optical pyrometer or thermal paints can be used. Thermocouples are easy to handle, but always measure their own temperature, so for reliable values the contact resistance to the target has to be minimized, which can be quite difficult without soldering. A pyrometer detects the thermal radiation within a solid angle, which makes it unsuitable for measurements in radiating flames such as in this work. Thermal paints show colour change associated with the mean or maximum temperatures, hence not suitable for real time surface temperature measurements. An alternative approach is the use of thermographic phosphor (TP) which offers high temporal and spatial resolution as well as good accuracy and precision [8]. The technique was adopted by Brübach *et al* [9] to measure the radial surface temperature profiles of the plate subjected to impinging flame jets. The reported surface temperature results were reliable with standard deviations of about 2 K. Fuhrmann *et al* [10] employed phosphor thermometry for 2D temperature distribution measurements of the exhaust valves in an optically accessible direct injection internal combustion

engine. Phosphor thermometry was the most preferable due to its semi-invasiveness and robustness against soot radiation and chemiluminescence, which occur in internal combustion engines. Euler *et al* [11] also measured the surface temperatures of the bluff body of a swirl burner using phosphor thermometry, and reported that the local surface temperature may affect the local heat transfer and gas temperatures. Mohammed *et al* [12] using TP thermometry measured the surface temperature of a flat and a cylindrical surface heated with a laminar, premixed ethanol/air flame. The authors reported higher stagnation heat fluxes for a cylindrical surface compared to a flat surface.

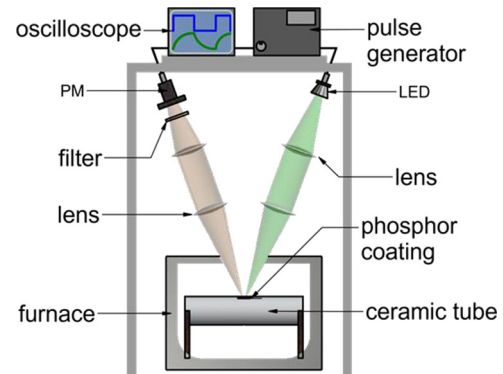
There are wide varieties of ceramic phosphors that survive harsh physical and chemical environments, are insoluble in water, durable and easy to apply. Each phosphor material selected for a particular application is highly sensitive within a specific range of temperatures. Seat and Sharp [13] reported that single-crystal ruby fibres were found to be potential candidates for dedicated temperature sensing from room temperature up to 923 K. The phosphor material (ruby) was used as a temperature sensor by Salem *et al* [7] to measure surface temperatures on a flat plate subjected to flame impingement. For the reported surface temperatures, reliable results were obtained with errors less than 5 K, and high heat fluxes recorded at the stagnation point.

TP materials generally consist of ceramic host materials doped with trace elements that emit light when suitably excited. To obtain the temperature, the surface wall of the substrate is coated with a thin layer of the phosphor material and excited by an energy light source. The subsequently emitted luminescence of the phosphor material can be exploited for surface thermometry, and based on the calibration data, the temperature can be quantified [14]. In most studies, the luminescence is normally excited using a pulsed laser with pulse duration in the nanosecond regime. However, the excitation using light emitting diodes (LED) in the microsecond range which greatly reduces the cost for such temperature measurements has been reported [15–17]. For the luminescence excitation using LED, Atakan *et al* [18] recommended appropriate measurement strategies in order to obtain high signal levels. The luminescence of the phosphor depends on temperature, so that either the phosphorescence decay times or the intensity ratios of two different emission lines can be exploited for surface thermometry [14]. The intensity ratio is mostly suited for 2D temperature measurements, and normally implemented with two detectors, hence, requires a carefully assembled setup. Dragomirov *et al* [19] using the spectral intensity ratio method reported 2D temperature measurements of spray-induced wall cooling with high spatial and shot-to-shot precision of 0.5 and 0.6 K respectively. The authors also reported that for quantitative analysis, a compromise between the coating thickness and the measurement accuracy is worthy consideration for applications where the rate of heat transfer is high. On the other hand, the phosphorescence decay times approach is most preferable for high accuracy and precision for the surface temperature measurements. Fuhrmann *et al* [20] compared the lifetime and the intensity ratio methods using  $Mg_4FGeO_6:Mn$  and reported improved precision for the former over the latter approach. The lifetime approach is the

preferable method and the luminescence decay signals can be captured with the aid of high-speed cameras or photomultipliers as detectors [14]. High-speed cameras image temperature distributions two-dimensionally, but this adversely increases the experimental efforts and costs compared to photomultipliers. Here, the phosphorescence decay times are evaluated for pointwise temperature measurements, due to the high accuracy and independence on the excitation intensity, as long as the phosphor decay follows an exponential law.

The gas phase temperatures can be measured with various techniques ranging from intrusive to non-intrusive. Yousefi-Asli *et al* [21] determined the flame temperature fields optically with the Mach–Zehnder interferometry for a methane/air flame impinging on a convex surface. The maximum temperature of the flue gases in the boundary layer, in vicinity of the wall, was taken as the reference temperature for calculation of the Nusselt number. Here, the question arises, whether this can be transferred to different situations, where no such sophisticated temperature measurement technique is available, so, will such a Nusselt number be useful? Salem *et al* [7] measured the flame temperatures using OH-laser induced fluorescence (LIF) thermometry, and found it difficult to obtain the gas phase temperature of methane/air flames near the flat impingement surface. This was due to the low level of OH concentration near the plate wall, caused by the relatively low temperatures, resulting in a very poor signal from OH-LIF. It was suggested that by using other methods like NO-LIF or coherent anti-stokes Raman spectroscopy (CARS), it might be possible to measure temperatures near the wall. Brübach *et al* [9] using the CARS technique, measured the flame temperature profiles of laminar flame impinging on a flat surface. The temperatures were obtained at distances of 300  $\mu\text{m}$  from the flat surface with shot-to-shot standard deviation of about 60 K. The technique is considered to provide the most accurate and precise gas phase temperature measurement. However, CARS process is a nonlinear optical phenomenon; hence, a requirement for high laser intensities to produce strong signals. In addition, the CARS signals can be affected by saturation effects. Moreover, due to the advanced nature of the setup, this technique is primarily used by specialist. Korobeinichev *et al* [22] and Skovorodko *et al* [23] showed the possibility of measuring flame temperature profiles with different types of Pt/Pt + 10% Rh thermocouples at distances of about 0.2 mm from the surface of the burner. The micro-thermocouples are easily used in flame temperature measurement. The current work seeks to explore the practicability of gas phase temperature measurements in laminar flames with micro-thermocouples near the impingement surface. The measured orthogonal gas-phase temperature- gradients near the impingement surface can be used for the determination of the local heat fluxes.

Considering the available literature, limited studies have employed phosphor thermometry for surface temperature measurement from flame impingement to cylindrical surfaces. In addition, the exit gas velocity relative to the flame speed has not been considered an important parameter in relation to heat transfer on curved surfaces. This work uniquely employs two techniques, i.e. micro-thermocouple for gas phase temperature measurement and TPs for surface



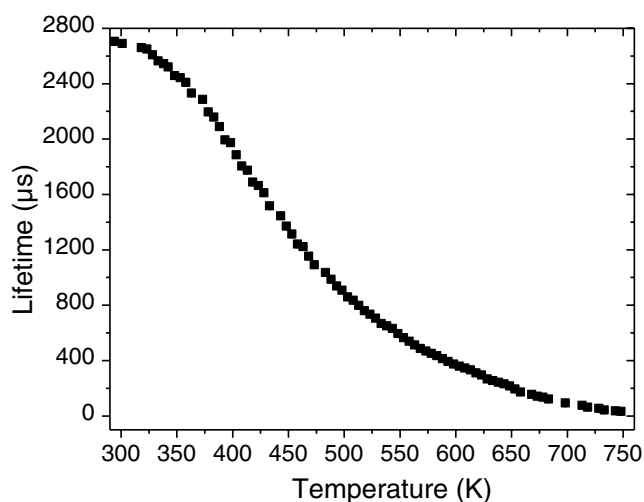
**Figure 1.** Wall surface temperature calibration on ceramic tube.

temperature determination. Through these measurements, the stagnation point heat flux of a nearly 1D flame is determined. Several parameter variations were investigated: The variation in cold gas velocities ( $0.1 \text{ m s}^{-1}$ – $0.5 \text{ m s}^{-1}$ ) relative to laminar flame speed, burner to target surface spacing ( $H/d = 0.5$ – $2$ ), which is taken as the ratio of the distance between the burner exit surface, and the impingement surface ( $H$ ) to the burner diameter ( $d$ ), are presented. The influence of the equivalence ratio ( $\Phi = 0.85$ – $1.2$ ), and curvature effects on heat transfer characteristics of flame impingement on a circular tube is investigated and compared to published work for flat surface flame impingement.

## 2. Methods

### 2.1. Ruby deposition and temperature calibration

The sol-gel method was used for thin film deposition with 1.1% chromium doped alumina, because Pfritsch *et al* [24] reported that such ruby films are most promising for temperature sensor applications, since they show high phosphorescence intensities. The ceramic tube was wetted with the liquid sol, subsequently annealed in air at 563 K to form an amorphous aluminium oxide ( $\text{Al}_2\text{O}_3$ ) film, and then annealed in an electric furnace in oxygen atmosphere for 2 h at 1350  $^\circ\text{C}$  for crystallization. A ceramic tube was selected (60% alumina and 40% silica) to withstand these high annealing temperatures. The deposited films obtained at the end of the procedure were analyzed with x-ray diffraction, it was confirmed that the phase formed is polycrystalline  $\alpha$ - $\text{Al}_2\text{O}_3$ . The coated ceramic tube was then calibrated for surface temperature measurement, by measuring the phosphorescence lifetime of phosphor excitation with a light pulse in a temperature-controlled electric furnace. The ceramic tube was placed inside the furnace as shown schematically in figure 1, and stepwise heated until constant temperatures were attained measured with K-type thermocouple. The temperature was increased from room temperature in steps of 5 K up to 750 K. For each set temperature, the time dependent emission signal of the phosphorescence was obtained and the decay time evaluated by fitting an analytical waveform to the decay curve signal using an algorithm by Brübach *et al* [25]. More details on phosphor excitation, signal acquisition and processing is explained in the subsequent setup on section 2.2.



**Figure 2.** Phosphorescence lifetimes of  $\text{Cr}^{3+}:\text{Al}_2\text{O}_3$  as a function of temperature.

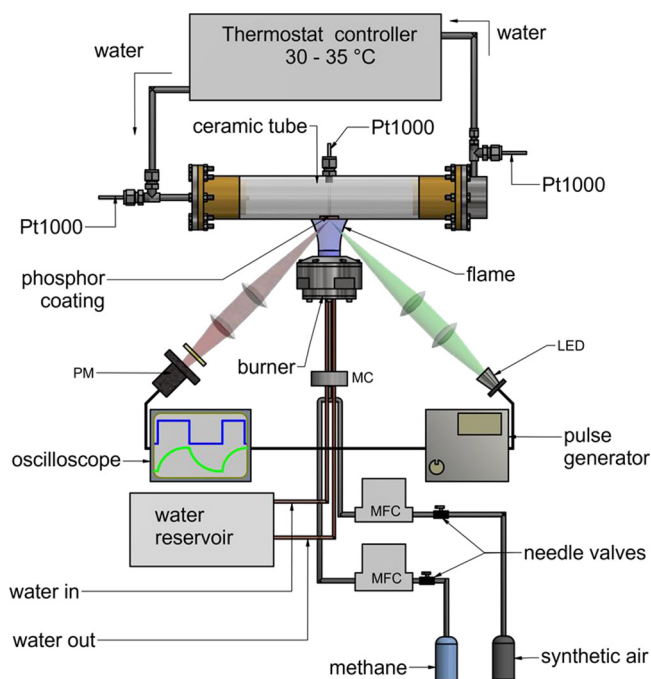
The temperature-dependence of the phosphorescence lifetime was determined only for the outer surface of the ceramic tube. The obtained lifetimes are plotted in figure 2 as a function of temperature ranging from 2.78 ms at 298 K to 62  $\mu\text{s}$  at 750 K.

The error bars are the standard deviation from three repeated measurements, which in this case are very small (figure 2), and show similar temperature dependence of the phosphorescence lifetime. The phosphorescence lifetime decreases as the temperature increases which is a typical behaviour for ruby [13]. Pflitsch *et al* [24] measured the phosphorescence lifetime of ruby deposited on silicon substrates for the temperature range 294 K to 833 K and obtained similar results.

## 2.2. Surface temperature measurement

The heat flux at the stagnation point was determined through the measurement of surface temperatures on the flame impingement side, and on the water-cooled backside. Figure 3 shows the schematic diagram of the flame jet impingement experimental setup used for the investigation. The temperature measurements were only carried out at the stagnation point.

A homemade sintered bronze burner of 30 mm diameter ( $d$ ) was used to establish a 1D flame. The burner was cooled with water flowing through a copper coil tube embedded in the sintered matrix. The laminar flame impinges on a water-cooled alumina tube with a wall thickness of 5 mm, an outer diameter ( $D$ ) of 60 mm and a length ( $L$ ) of 250 mm. The ceramic tube was coated with ruby as a phosphor on the region where stagnation measurements were to be made. The cooling water enters the ceramic tube through an axial 12 mm central opening on one side of the flange, and leaves through the other flange in a radial direction, also with an opening of 12 mm. This construction ensures that the ceramic tube is always filled with cooling water. The flow of the cooling water was maintained at 0.36 liters per minute (LPM) constant flow rate, and with temperature between 30 °C–35 °C with a thermostat controller. Three Pt1000 temperature sensors were used to measure the temperature of the water at the inlet, at the outlet,



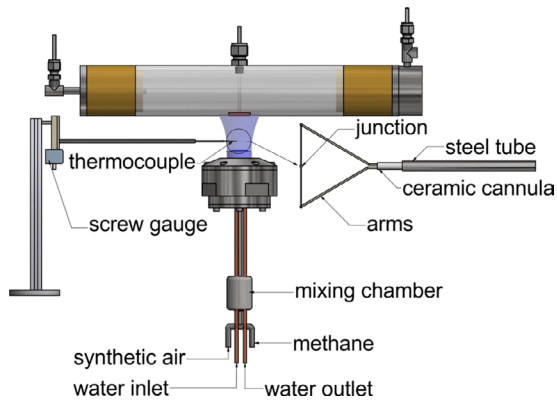
**Figure 3.** Wall temperature measurements from methane/air flame impingement.

and at the backside of the stagnation point. For the measurement of the temperature on the flame side, the phosphor coating was excited with a LED array (Opto Technologies Inc., OTLH-0020-GN) at a wavelength of 532 nm. A fast pulse generator (Toellner, TOE7404) was used to provide the current input for the LED and to control the temporal excitation intensity shape. A rectangular light pulse of 20 ms duration was used for the excitation. The emitted phosphorescence signals from the measurement area were focused with lenses through a band pass filter onto a photomultiplier (PM) tube (Hamamatsu H6780-03). The signals were recorded by a digital oscilloscope (Tektronix TFS 2024) and transferred to a personal computer after averaging for 128 pulses. The lifetime measurements with the burning flame were taken after the outlet temperature of the cooling water became constant.

A first set of experiments was conducted to study the effects of variation of cold gas velocity (0.1  $\text{m s}^{-1}$ –0.5  $\text{m s}^{-1}$ ) on stagnation point heat flux for three equivalence ratios, lean ( $\Phi = 0.85$ ), stoichiometric ( $\Phi = 1.0$ ) and rich ( $\Phi = 1.2$ ) at a separation distance,  $H/d = 0.5$ . This distance is denoted as the axial distance along the burner axis measured from the exit plane of the burner to the target point on the ceramic tube. The second set of experiments were carried out to investigate the effect of varying  $H/d$  (0.5–2) at  $\Phi = 1.0$ . In all cases, measurements were repeated three times in order to estimate the deviations.

## 2.3. Flame temperature measurement

The gas phase temperature profiles were measured from the burner surface to the impingement surface. The measured temperature profiles for cold gas velocities 0.1  $\text{m s}^{-1}$  to 0.5  $\text{m s}^{-1}$  help in the understanding and visualization of the



**Figure 4.** Gas phase temperature measurement with thermocouple.

changes in the flame stabilization mechanism. In addition, the temperature gradients of the gas phase near the impingement surface can be used as a second method for the determination of the stagnation point heat flux. The gradient measurements were only conducted for stoichiometric condition at a fixed burner to impingement surface distance ( $H/d = 0.5$ ), while some gas phase temperatures at this distance were also measured for the other equivalence ratios at  $v = 0.1 \text{ m s}^{-1}$ . The moving thermocouple system was used in the measurements of the axial temperature distributions as shown schematically in figure 4. The thermocouple of type R (Pt/Pt + 13%Rh), used for gas phase temperature measurements was coated with a thin layer ( $\sim 10 \mu\text{m}$ ) of  $\text{SiO}_2$ , to prevent surface catalytic processes. Here, the process of cleaning, and coating the thermocouple was carried out as described by Skovorodko *et al* [23]. A thermocouple with a wire diameter of  $130 \mu\text{m}$  and a junction diameter of  $190 \mu\text{m}$  was selected. The thermocouple arms made from  $200 \mu\text{m}$  wire diameter were  $30 \text{ mm}$  long, and fixed in a ceramic cannula of  $4 \text{ mm}$  outer diameter. The ceramic cannula was placed inside a stainless steel tube of  $6 \text{ mm}$  diameter. Both together were fixed on a movable device with a micrometre screw gauge for vertical measurements (see inset in figure 4). This allowed the thermocouple to be traversed vertically through the flame to obtain axial temperature profiles of the flame. The measured temperatures were corrected for radiation losses of the thermocouple using the formula given by Kaskan [26].

In all the experiments, flow rates of the gas components of the unburned mixture were set to within  $\pm 1\%$  by mass flow controllers (MKS Instruments Inc.). The reactants flow rates at the outlet from the mass flow controllers (MFC) were calibrated using a bubble flow meter (Gilian, Gilibrator) to confirm the claimed accuracy. Methane with  $99.5\%$  purity was used and burnt with synthetic air (volume:  $21\% \text{ O}_2$  and  $79\% \text{ N}_2$ ).

### 3. Temperature and heat flux analysis

The surface temperature difference through the ceramic wall was used for the determination of the heat flux at the stagnation point. On the flame side, the surface temperature was measured with phosphor thermometry as discussed above.

**Table 1.** Thermal resistance of ceramic material and ruby coating.

Material	Thermal conductivity, $\lambda$ ( $\text{W m}^{-1} \cdot \text{K}^{-1}$ )	Thickness, $x$ (m)	Resistance, $R = \frac{x}{\lambda}$ ( $\text{K w}^{-1}$ )
Ceramic	3.4	$5 \times 10^{-3}$	$1.47 \times 10^{-3}$
Ruby	28	$10 \times 10^{-6}$	$3.5 \times 10^{-7}$

The lifetime was determined by fitting an exponential function (1) to the signal, which describes the signal shape:

$$I(t) = I_0 \cdot \exp\left(\frac{-t}{\tau}\right). \quad (1)$$

Here,  $I(t)$  is the intensity of the decaying phosphorescence signal,  $I_0$  is the initial phosphorescence intensity at time  $t = 0$ ,  $t$  is the time since cessation of excitation source and  $\tau$  is the phosphorescence lifetime.

The thickness of TP layers may have a significant effect on the phosphorescence signal [27]. Stronger phosphorescence signals from thicker coating layers are favourable for the surface temperature measurement accuracy [19]. However, thicker coating lead to temperature gradients within the phosphor layers, which in turn can influence the heat transfer. Knappe *et al* [28] investigated the phosphor thickness dependent on surface temperature in transient combustion environments. They reported that, a phosphor coating above  $20 \mu\text{m}$  layer thickness experiences a thermal gradient for the considered engine temperatures, whereas thinner layers seems unaffected within the limits of measurement accuracy and precision. On the other hand, Atakan and Roskosch [29] reported that the maximum surface temperature in unsteady heat transfer processes is influenced even by relatively thin layers. Here, the thickness of the coating used is  $10 \mu\text{m}$ ; the resistance across the ruby coating was calculated and compared to the one across the ceramic tube wall and the results are tabulated in table 1. The results indicate a considerably smaller thermal resistance for the ruby coating compared to that of the ceramic tube. Therefore, the overall local heat transfer at the stagnation point will be minimally influenced by the  $10 \mu\text{m}$  thickness of the coating material, hence it is not considered in the evaluation of heat fluxes.

The heat flux at the stagnation point was evaluated with Fourier's law for 1D steady state conditions as expressed in (2):

$$\dot{q} = \frac{\dot{Q}}{A} = \frac{\lambda(T_f - T_w)}{r_2 \ln \frac{r_2}{r_1}} \quad (2)$$

where,  $\dot{q}$  is the heat flux,  $T_f$  is the temperature measured at the flame side,  $T_w$  is the temperature on the water-cooled side,  $r_2$  and  $r_1$  are the outer and inner tube radius of the ceramic tube respectively,  $\lambda$  is the thermal conductivity of the ceramic tube. The 1D heat transfer is applicable, since heat fluxes were only measured along the symmetry line, which ensures that there is no heat flux in perpendicular direction. The thermal conductivity of the ceramic material was measured with the NETZSCH LFA 457 Micro-flash as specified in ASTM E 1461. The thermal diffusivity of the ceramic material was

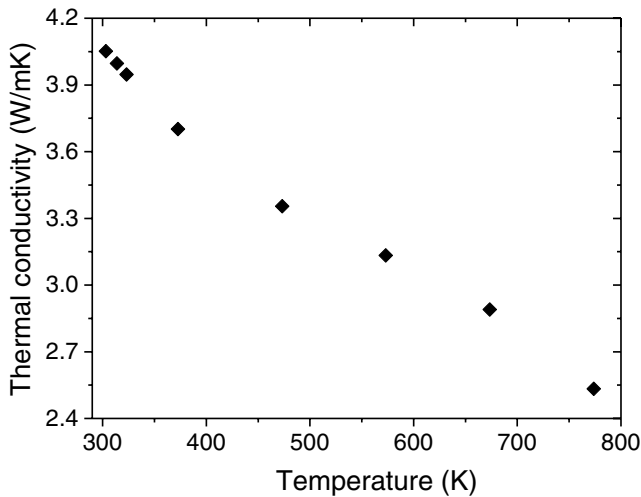


Figure 5. Thermal conductivity of the tube material.

measured in a vacuum environment. The measurements were carried out by subjecting the test specimen to a high intensity, short duration thermal pulse from a laser on the front surface, and monitoring the temperature change at the rear surface as a function of time using an IR detector. Thermal diffusivity was calculated using the average of several pulses based on the specimen thickness, and the time required for raising the temperature of the test specimen's back surface by a certain percentage of its maximum. The test specimen diameter was 12.7 mm with thickness of 4 mm. The thermal diffusivity was determined from (3):

$$\alpha = \frac{\kappa_{\chi} \cdot L^2}{t_x} \quad (3)$$

where  $\alpha$  is the thermal diffusivity,  $\kappa_{\chi}$  is the constant dependent on  $x$ -percent temperature rise,  $L^2$  is the thickness of specimen, and  $t_x$  the time for the rear surface temperature to rise to  $x$ -percent of its maximum value.

Then the thermal conductivity obtained from (3) as expressed below by (4):

$$\lambda = \alpha \cdot \rho \cdot c_p. \quad (4)$$

Here,  $\lambda$  is the thermal conductivity,  $\rho$  the density of ceramic sample, and  $c_p$  the specific heat capacity of the ceramic sample. The specific heat capacity of the ceramic sample was required in equation (4) to determine the thermal conductivity from diffusivity, and so it was measured by comparing the temperature rise during the diffusivity measurement of the ceramic sample to the temperature rise of Pyroceram 9606, which was used as the reference, and calculated by (5):

$$c_{p(\text{sample})} = \frac{(m \cdot c_p \cdot \Delta T)_{\text{reference}}}{(m \cdot \Delta T)_{\text{sample}}} \quad (5)$$

where  $c_p$  is the specific heat,  $m$  the mass and  $\Delta T$  is the temperature change.

The evaluated thermal conductivity of the ceramic sample as a function of temperatures is plotted in figure 5; it decreases as the temperature increases for the measured temperature range.

The stagnation point heat flux was also determined from the flame temperature gradients of the gas phase near the impingement surface, using equation (6). With the existence of a thin thermal boundary layer at the surface, the heat transfer was taken to be by pure conduction:

$$\dot{q}_{\text{conv}} = \dot{q}_{\text{cond}} = -\lambda_{\text{mix}} \left. \frac{\partial T}{\partial r} \right]_{r=r_2} \quad (6)$$

where  $(\partial T/\partial r)_{r=r_2}$  represents the temperature gradient at the surface, and  $\lambda_{\text{mix}}$  is the thermal conductivity of combustion products at the surface temperature, taken from equilibrium compositions.

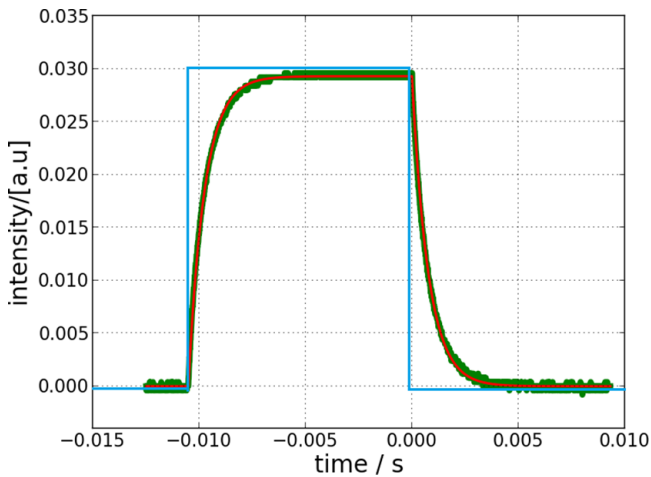
#### 4. Uncertainty analysis

The uncertainties in the measured and calculated parameters was carried out using the method suggested by Kline and McClintok [30]. The relative error from the lifetime measurement during calibration were below 0.8% at temperatures below 750 K, and the errors in the temperature estimated to be below 3–5 K depending on the exact temperature. Uncertainties in the thermal conductivity of the alumina and the equivalence ratio were 1.4% and 2.3% respectively [31]. The maximum uncertainty in the heat flux measurements was 7.1%. The accuracy of the K-type thermocouple for temperature calibration was  $\pm 2$  K while the error of the thermocouple for flame temperature measurements was within  $\pm 45$  K. This was determined from the scatter of four measurements of temperature profile.

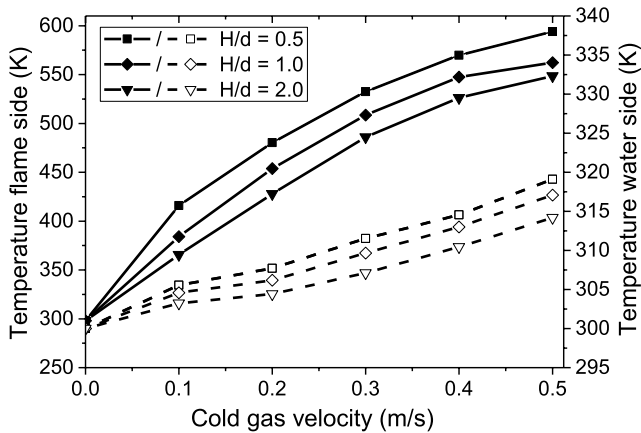
#### 5. Results

##### 5.1. Surface temperature measurements

Methane/air flames of three different equivalence ratios: lean ( $\Phi = 0.85$ ), stoichiometric ( $\Phi = 1.0$ ) and rich ( $\Phi = 1.2$ ) were investigated for five different burner to tube distances ( $H/d$ ). The water side temperatures measured with the Pt1000 temperature sensor while, the surface temperatures on the flame impinging side determined from the excitation of chromium-doped alumina. The thickness of the coating was kept at approximately 10  $\mu\text{m}$ , calculated from the change in mass of the ceramic tube during the sol-gel deposition (16.5 mg), the area of deposition (4  $\text{cm}^2$ ) and the density of  $\alpha\text{-Al}_2\text{O}_3$  (3.99  $\text{g cm}^{-2}$ ). Pilgrim *et al* [32] reported sensor layer thickness below 35  $\mu\text{m}$ , showed less than 1% differences between the measured temperature and the surface temperature. However, the emission intensity is reduced substantially. Therefore, a compromise must be sought between measurement accuracy and signal amplitude. Knappe *et al* [28] reported thicker phosphor layers above 20  $\mu\text{m}$  showed a delayed temperature response at the wall side and experienced a substantial thermal gradient. Here, the 10  $\mu\text{m}$  phosphor thickness deemed sufficient because high phosphorescence signal levels are achievable. As an example, a typical time dependent phosphorescence signal is shown in figure 6, where the green curve is the measured phosphorescence decay time signal stored by an



**Figure 6.** Lifetime analysis on flame side (blue: LED intensity, green: measured curve, red: fitted curve).

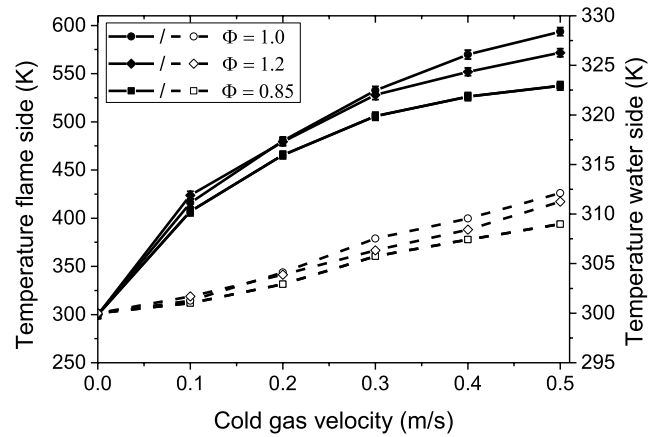


**Figure 7.** Surface temperature for three burner to tube distances for stoichiometric flames (solid symbols: flame side, hollow symbols: water-cooled side).

oscilloscope, and the red curve is the fitted analytical waveform. A rectangular light pulse (blue line) of 20ms duration was used for excitation. The signal is an average of the phosphorescence signal after excitation with 128 LED light pulses. A detailed analysis on the pulse width selection is published elsewhere [18]. The signal to noise ratio was very good for all the measurements. A lifetime of 766  $\mu\text{s}$  is obtained from the shown curve leading to a temperature of 517 K deduced from the calibration curve figure 2.

Figure 7 shows the surface temperature measurement as a function of cold gas velocity on both sides of the ceramic tube at the stagnation point. Again, the temperatures on the flame side were measured with TPs while, on the water-cooled side a Pt1000 temperature sensor was used. The results in the figure 7 are for stoichiometric conditions for three separation distances, i.e.  $H/d = 0.5, 1$  and  $2$ , out of the five separation distances ( $H/d = 0.5, 0.75, 1, 1.5$  and  $2$ ) measured.

The temperature increases much stronger on the flame side as the fresh gas mixtures increases, while on the water-cooled side, the temperatures are almost constant. Higher temperatures are recorded for the smallest separation distance ( $H/d = 0.5$ ). As the separation distance is increased from



**Figure 8.** Surface temperature for three equivalence ratios ( $\Phi = 0.85\text{--}1.2$ ) at  $H/d = 0.5$  (solid symbols: flame side, hollow symbols: water-cooled side).








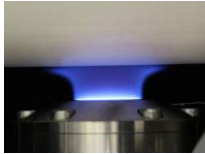




$H/d = 0.5$  to  $H/d = 2$  the temperature decreases. Upon the increase of the mass fluxes of the fresh gases, the temperature differences through the wall increases, and hence the heat flux. Considering  $H/d = 0.5$ , for the water side the temperatures vary between 306 K to 319 K, while on the flame side between 416 K to 594 K. The observed small temperature change on the water-cooled side is due to the high heat transfer coefficient of the cooling water and the high water mass flow rate ( $0.36\text{ l min}^{-1}$ ). On the flame side two effects contribute to the increase in the heat flux, and thus to the temperature, with the velocity of the reactant gas mixture on one side, the boundary layer gets thinner, increasing the temperature gradients. On the other side, and probably more important, the heat losses to the burner get smaller with fresh gas velocities approaching the burning velocity, leading to higher temperatures and thus, again to higher temperature gradients of the burnt gases impinging on the surface.

In figure 8 the surface temperatures at  $H/d = 0.5$  for three equivalence ratios ( $\Phi = 0.85, 1.0$  and  $1.2$ ) are compared, the stoichiometric flame has the highest surface temperatures at higher velocities while, the lowest surface temperatures are observed for lean conditions. This can in part be attributed to the adiabatic flame temperatures which are 2101 K, 2250 K and 2171 K for the lean, stoichiometric and rich flames respectively. The order of the heat fluxes follows the order of the adiabatic flame temperatures, as soon as the cold gas velocity approaches the burning velocity. For low cold gas velocities between  $0.1$  and  $0.3\text{ m s}^{-1}$ , the surface temperatures measured on the flame side for the rich and stoichiometric flames are almost the same, and slightly lower for the lean flame (figure 8).

From thermocouple measurements within the burner it is found qualitatively that the heat flux to the burner at low cold gas velocities are highest for the stoichiometric flame, leading to a reduction in flame temperature, as also reported below. At flow rates above  $0.3\text{ m s}^{-1}$ , the heat flux to the burner is no longer depending on the equivalence ratio and the heat fluxes follow the adiabatic flame temperature for comparable conditions. Salem *et al* [7] reported similar observations of close surface temperatures between rich and stoichiometric

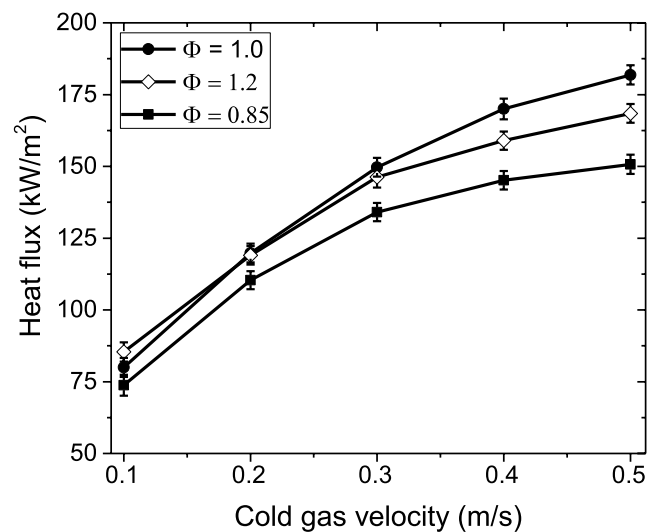


**Table 2.** Photographs of methane/air flame impinging on tube for  $\Phi = 0.85$ – $1.2$  at  $H/d = 0.5$ .

	$\Phi = 1.0$	$\Phi = 1.2$	$\Phi = 0.85$
$v = 0.1 \text{ m s}^{-1}$			
$v = 0.2 \text{ m s}^{-1}$			
$v = 0.3 \text{ m s}^{-1}$			
$v = 0.4 \text{ m s}^{-1}$			

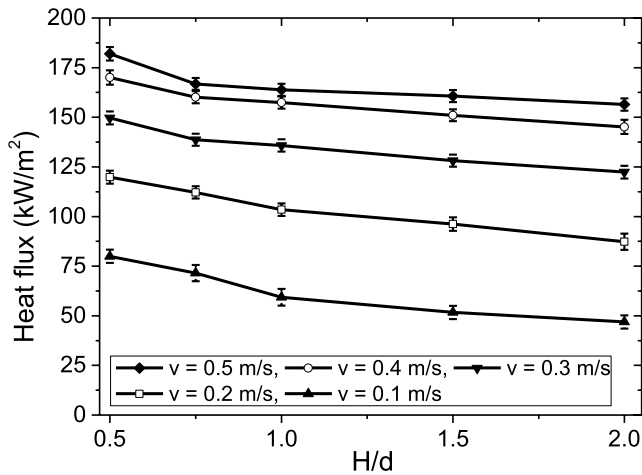
flames for methane/air flame impinging on a flat surface for  $H/d = 0.5$ . It was initially supposed that, since the flame was burning at ambient conditions, additional air might have entrained resulting in lower real stoichiometries. However, similar trends regarding heat flux are found in 1D simulations without air entrainment. The authors concluded that, the investigated distance  $H/d = 0.5$  was quite small, hence the effect of air entrainment played a minor role in change of stoichiometry.

Photographs of lean, stoichiometric and rich methane/air flames impinging on the ceramic tube, which mainly show the CH luminescence, reveal that at velocity of  $0.1 \text{ m s}^{-1}$ , the rich flame is more stretched towards the tube (table 2), compared to the other equivalence ratios. For the stoichiometric and the lean flame, the reaction zone is very near to the burner, and only the hot combustion gases impinge on the ceramic tube. The rich flame has a lower burning velocity ( $0.43 \text{ m s}^{-1}$ ) compared to stoichiometric flame ( $0.48 \text{ m s}^{-1}$ ). This results to a larger separation of the flame front from the burner, thus lower heat losses to the burner for  $\Phi = 1.2$  than for  $\Phi = 1.0$ . The measured maximum flame temperatures at a velocity of  $0.1 \text{ m s}^{-1}$  (figure 12), presented later, reveals almost the same maximum flame temperatures for  $\Phi = 1.2$  and  $\Phi = 1.0$ , while the lean flame temperature is slightly lower. Above a velocity of  $0.3 \text{ m s}^{-1}$  both the rich and stoichiometric flames are stronger detached from the burner thus, heat losses to the burner are reduced (table 2). Here, the surface temperature is strongly influenced by the adiabatic flame temperature, hence high temperatures for stoichiometric flame. Similarly, the measured maximum flame temperatures with micro-thermocouple at a cold gas velocity of  $0.4 \text{ m s}^{-1}$  shows highest temperatures for the stoichiometric flame followed by the rich flame, with lowest for the lean flame.

**Figure 9.** Stagnation point heat fluxes at  $H/d = 0.5$  for  $\Phi = 1.0$ .

### 5.2. Stagnation point heat fluxes

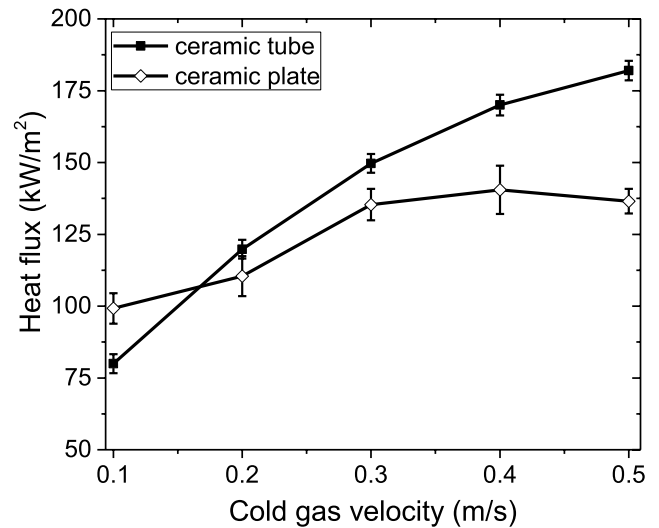
The temperature difference between the water-cooled side and the flame side for the various exit gas velocities ( $0.1 \text{ m s}^{-1}$ – $0.5 \text{ m s}^{-1}$ ) from figure 8 are used for the calculation of the heat fluxes. Fourier's law for 1D steady state conditions is used for its evaluation. Since, the water-cooled side temperatures remain virtually constant as explained earlier; the heat flux trends all follow the trends in flame side surface temperature. Figure 9 shows the variation on heat flux as a function of cold gas velocity, for methane/air flame impinging on a ceramic tube for various values of  $\Phi$  (0.85–1.2), and at  $H/d = 0.5$ . In all cases, heat fluxes increases with the cold gas velocity. The stagnation point heat flux is lowest for  $\Phi = 0.85$ , ranging



**Figure 10.** Heat fluxes at  $H/d = 0.5$ – $2.0$  for a stoichiometric flame.

from  $74 \text{ kW m}^{-2}$  to  $151 \text{ kW m}^{-2}$ . This can be attributed to the low adiabatic flame temperature for  $\Phi = 0.85$  resulting in low gas temperatures impinging on the ceramic tube. At cold gas velocities below  $0.3 \text{ m s}^{-1}$ , the heat fluxes of flame at  $\Phi = 1.2$  are almost equal to the ones of stoichiometric flame. But as the cold gas velocities increase above a velocity of  $0.3 \text{ m s}^{-1}$ , the surface temperatures are highest for the stoichiometric case, and hence the heat flux. Dong *et al* [1, 33] reported higher flame to surface heat fluxes for fuel-rich conditions. Chander and Ray [6] explained higher heat flux for rich flames in terms of initially rich mixture ( $\Phi = 1.2$ ) possibly becoming nearly stoichiometric due to air entrainment from the surrounding. This does not appear to be a suitable explanation for the present findings at relatively low burner to surface distances. As explained earlier the main reason for almost the same heat fluxes for rich and stoichiometric flames at lower cold gas velocities is found in the differences in burning velocities and not in air entrainment.

The heat flux does not increase linearly with the cold gas velocity; instead, there is a change of slope around velocities of  $0.4 \text{ m s}^{-1}$  for the stoichiometric flame, and around  $0.3 \text{ m s}^{-1}$  for the rich and lean flames. Mohammed [12] also reported a slope change for laminar premixed ethanol/air flames impinging on cylindrical surface. This change can easily be understood in terms of flame stabilization mechanisms, i.e. when the cold gas velocity is below the laminar burning velocity ( $0.48 \text{ m s}^{-1}$ ,  $0.43 \text{ m s}^{-1}$  and  $0.4 \text{ m s}^{-1}$  for stoichiometric, rich and lean methane/air flames respectively), the flame will be stabilized on the burner surface. In this regime, the heat transfer is influenced strongly by the mass flow rate, because of the large heat flux to the burner, which is reduced with increasing cold gas velocity. As soon as the cold gas velocity is above the laminar burning velocity, the stabilization mechanism changes to wall stabilized (flame detached from the burner). Here, the dependence of the heat flux on fresh gas velocity is much lower, because the heat losses to burner is minimal. At these higher velocities, the boundary layer thickness at the stagnation point is slightly decreasing with the increasing gas velocity, and influences the heat transfer rate at the stagnation point only



**Figure 11.** Heat flux at the stagnation point for a ceramic tube and a ceramic plate at  $H/d = 0.5$  for stoichiometric condition.

slightly. Instead, there is a higher mass flux in the radial and circumferential directions along the wall jet region.

The effects of the separation distance, i.e.  $H/d = 0.5$ – $2$  on the stagnation point heat flux for stoichiometric conditions were also investigated as presented in figure 10. Due to optical inaccessibility, investigations at smaller separation distances, below  $H/d = 0.5$  were not possible. The separation distance is an important parameter concerning the heat transferred to the impingement surface, and flame stabilization. The heat flux at the stagnation point is highest for the smallest  $H/d = 0.5$  and slightly decreases as the separation distance is increased from  $H/d = 0.5$  to  $2$ . This can be explained by the closeness of the ceramic tube to the hottest region of the flame with high temperature. This causes the heat flux to increase, and due to closeness of the flame to the impingement surface there is minimal heat losses to the surroundings. When  $H/d$  is increased, the flame moves away from the impingement surface, the orthogonal flow velocity drops, and at large distances, even the combustion gases impinging on the ceramic tube may get thermally diluted with the ambient air. Considering a fixed separation distance of  $H/d = 0.75$ , the heat flux increases from  $71 \text{ kW m}^{-2}$  to  $167 \text{ kW m}^{-2}$  as the reactants velocity increases from  $0.1 \text{ m s}^{-1}$  to  $0.5 \text{ m s}^{-1}$ . It is evident from figure 10 that at cold gas velocities of  $0.4 \text{ m s}^{-1}$  and  $0.5 \text{ m s}^{-1}$  that, the stagnation point heat flux is weakly influenced by the increase of the mass flux.

### 5.3. Comparison of stagnation point heat flux for a flat ceramic plate and a ceramic tube

Figure 11 shows the curvature effect on stagnation point heat flux for methane/air flame impinging on a ceramic tube and a ceramic plate at  $H/d = 0.5$  and for  $\Phi = 1.0$ . The compared heat fluxes for the ceramic plate is from the work of Salem *et al* [7], who measured the surface temperatures with phosphor thermometry at the stagnation point, similar to our study. The used disc for the flat surface was almost pure alumina

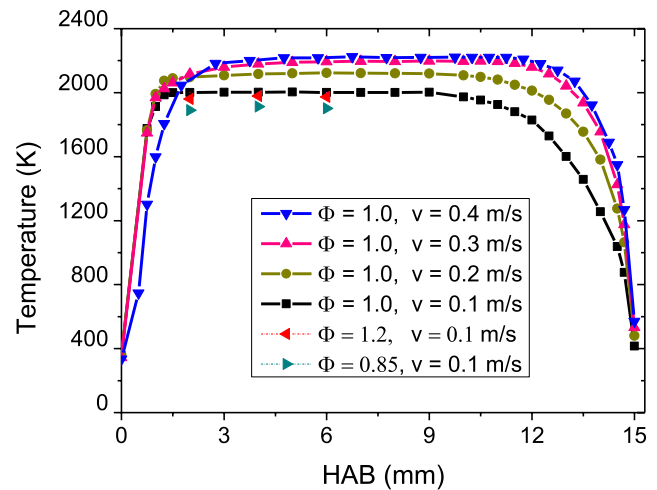
(94%) while the ceramic tube used in the present study is from 60% alumina and 40% silica. In both cases, a sintered matrix burner of diameter 30 mm was used.

Above cold gas velocity of  $0.2 \text{ m s}^{-1}$ , the heat fluxes are higher for the flame impinging on the tube compared to the flat plate geometry. Mohammed [12] observed similar trends for stagnation point heat flux for ethanol/air flames jet impingement cases. He explained the results in terms of the thickness change of the thermal boundary layer. For cold gas velocities above  $0.2 \text{ m s}^{-1}$  the flat surface offers flow restrictions to the combustion products once they impinge on the surface. The combustion products can only flow in the radial direction, and hence the formed boundary layer is thicker. For the cylindrical surface the impingement flame or the hot combustion gases can easily flow around the curved surface. The curvature allows both flow in the radial and the circumferential direction, resulting in a thinner thermal boundary layer, and hence a higher heat flux. However, no clear explanation was given as to why the heat fluxes were higher for a flat surface for low flow velocities below  $0.2 \text{ m s}^{-1}$ . Chander and Ray [6], and Van der Meer [34] stated that the higher stagnation point heat flux for a cylindrical surface is a result of a higher radial velocity gradient of the burnt gases just outside the boundary layer when compared to a flat surface. This is because the burnt gases can easily flow away in radial and angular directions from the stagnation point.

Wang *et al* [35] explained that higher heat transfer at the stagnation point is achievable from smaller cylinders if they are placed inside the potential core of the impingement jet. Whereas, for larger cylinders higher heat transfer is obtained outside the potential core. Giralt *et al* [36] explained the potential core length as the distance from the nozzle exit to an axial point where the centreline velocity is 98% of the jet exit velocity. Inside the potential core the small cylinder experiences a uniform-like incoming flow whereas, outside the potential core the small cylinder experiences a non-uniform free-stream flow with its axial velocity varying along the radial axis. Due to this reasoning, they concluded that inside the potential core, the highest stagnation heat transfer is obtained on small cylinders. On the contrary, outside the potential core as the cylinder diameter increases to approach that of a flat surface, it leads to higher stagnation point heat transfer. Considering a typical photograph of the flame impinging on a ceramic tube, as shown in table 2, may help to follow this argument line: At a velocity of  $0.1 \text{ m s}^{-1}$  it is seen that the tip of the potential core is far away from the impingement surface. Since the hot combustion gases are seen to impinge on the surface, this probably explains why the tube leads to a lower heat flux than the plate. As the cold gas velocity is increased to above  $0.2 \text{ m s}^{-1}$ , the flame is impinging on the surface, and the ceramic tube is inside the potential core of the jet. Also at higher cold gas velocities, the further reduction of the thermal boundary layer may lead to higher stagnation point heat fluxes for the tube.

#### 5.4. Flame temperature measurement

For the stoichiometric condition, the temperature profiles in the gas phase of the methane/air flame impinging on a

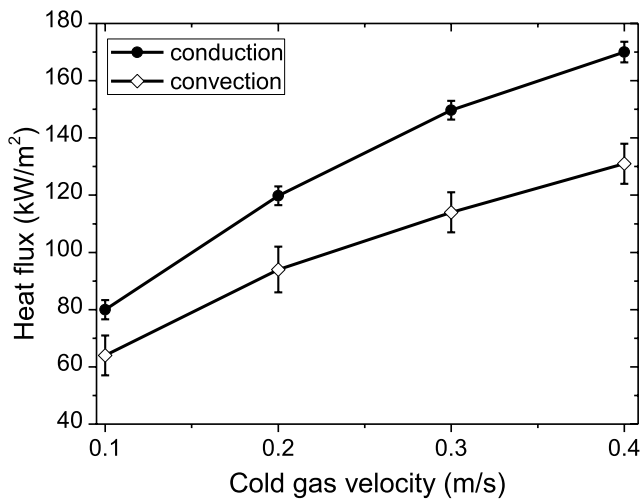


**Figure 12.** Flame temperature at  $H/d = 0.5$  for different  $\Phi$  and velocities, as indicated.

water-cooled tube were measured with a thermocouple of type R. Figure 12 shows the obtained temperature profiles at height above burner (HAB) = 15 mm for four selected cold gas velocities. In addition, for the other two equivalence ratios some exemplary points of the profiles were measured at the low cold gas velocity of  $0.1 \text{ m s}^{-1}$ , in order to prove the influence of heat losses to the burner. The gas phase temperatures were measured to a distance of approximately 0.3 mm to both surfaces, and the temperature profiles were extrapolated to the respective burner surface temperatures and to the ceramic tube surface temperatures, as measured. The lower cold gas velocities ( $0.1 \text{ m s}^{-1}$ – $0.3 \text{ m s}^{-1}$ ) are far below the laminar flame velocity of  $0.48 \text{ m s}^{-1}$  for a stoichiometric methane/air flame. It can be seen that the temperature rises steeply adjacent to the burner, an indication of large heat losses to the burner. The heat losses contribute to the reduction of the maximum flame temperature, the lowest flow velocity ( $v = 0.1 \text{ m s}^{-1}$ ) leads to the lowest maximum flame temperature of  $2021 \pm 23 \text{ K}$ . As the cold gas velocity is increased to  $0.4 \text{ m s}^{-1}$ , it tends to approach the laminar flame velocity of  $0.48 \text{ m s}^{-1}$ , the flame starts to detach itself from the burner. The temperature gradient becomes smaller for  $0.4 \text{ m s}^{-1}$  indicating lower heat loss to the burner. The flame stabilization changes from burner to wall stabilization approaching the laminar flame velocity.

At low cold gas velocities, it is seen that the flame temperatures for the three equivalence ratios are very near to each other, being slightly lower for the lean flame, showing the importance of the heat losses to the burner. The losses are highest for the flame with the largest laminar flame velocity, which is the stoichiometric one. This fits well to the measured wall temperatures and wall heat fluxes for these conditions presented above. Salem *et al* [7] simulated the temperature profiles for methane/air flames impinging on a flat surface. The change of stabilization mechanism from burner to plate was also reported, where a change of slope is observed at mass flux of around  $0.5 \text{ kg (m}^2 \text{ s)}^{-1}$  for their 1D geometry.

The gas phase temperature gradients near the stagnation point were only measured for the stoichiometric flame. They



**Figure 13.** Stagnation point convective and conductive heat flux at  $H/d = 0.5$  for  $\Phi = 1.0$ .

are highest for velocity of  $0.4 \text{ m s}^{-1}$  and lowest for velocity  $0.1 \text{ m s}^{-1}$ . The temperature gradient at first increases as the cold gas velocity increases until the differences for the tube stabilized flame gets relatively small. Initially, it was aimed to measure the gas phase temperatures at distances of less than  $0.2 \text{ mm}$  to the ceramic tube, and to determine the heat flux from it, but the closest temperatures obtained, were at approximately  $0.3 \text{ mm}$  to the impingement surface. This was evident from the manually operated micrometre screw gauge used for vertical movement of the thermocouple that, accurate measurement at smaller distances near the impingement surface were not possible. The problem may in part be overcome by using an automated stepper motor with an optical control system, which may be incorporated in future.

From figure 12, the stagnation point heat fluxes by convection from the flame impinging on the ceramic tube were calculated using equation (6). The temperature gradients were determined from the last points of the temperature profiles measurement with the thermocouple, and the surface temperatures on the ceramic tube measured from thermographic phosphors, and compared with the conductive heat fluxes across the walls of the ceramic tube determined with equation (2), and the results plotted in figure 13.

It is expected that, the convective heat transfer from the flame should be equal to the conductive heat transfer across the walls of the tube from the theory of thermal boundary layer [37]. Here, the convective heat transfer is measured to be lower than conductive one. The former is ranging from  $64 \text{ kW m}^{-2}$  to  $131 \text{ kW m}^{-2}$ , and the latter from  $80 \text{ kW m}^{-2}$  to  $171 \text{ kW m}^{-2}$ . However, the convective heat transfer rate is directly related to the temperature gradient at the selected distance from the tube. Therefore, the shape of the temperature profile in the thermal boundary layer dictates the convective heat transfer from the flame to the tube. In this study, the temperature gradients were determined at  $0.3 \text{ mm}$  from the surface of the tube, leading to lower temperature gradients, and hence lower convective heat transfer than conductive as shown in figure 13. For a better comparison, temperature gradients at distances less than  $0.2 \text{ mm}$  to the surface of the

tube should be used, which were not achievable with our setup as explained earlier. It is probably expected that close to the tube higher temperature gradients are obtainable resulting to higher convective heat transfer, possibly same to the conductive heat transfer.

## 6. Conclusions

The heat flux at the stagnation point from methane flames impinging on the cylindrical surface was investigated experimentally and compared with previous studies reported for flames impinging on flat surface. Phosphor thermometry was used for accurate surface temperature determination at the stagnation point. Moreover, for stoichiometric flames a coated thermocouple of type R was employed for the measurement of the flame temperature profiles at the separation distance of  $15 \text{ mm}$  between the burner and the impingement surface. The effects of cold gas velocity relative to the laminar flame velocity, equivalence ratio ( $\Phi$ ), the distance between burner to the cylindrical surface ( $H/d$ ) and surface curvature on heat flux studied. The main results of this article can be summarized as follows:

- (i) The surface temperatures from flame impingement can be evaluated from the phosphorescence lifetime of ruby, and hence such coatings are useful as surface temperature sensors. The sol-gel method can easily be used to prepare those thin films.
- (ii) The maximum heat flux is obtained for the smallest burner to impingement surface spacing, i.e.  $H/d = 0.5$  due to the high temperature of impinging flame jet at that distance and thereafter, as  $H/d$  is increased to 2 the heat flux declined.
- (iii) The stoichiometric flames lead to higher stagnation point heat fluxes, because of their high adiabatic flame temperatures for cold gas velocities greater than  $0.3 \text{ m s}^{-1}$ . On the contrary, below  $0.3 \text{ m s}^{-1}$  rich flames show similar heat fluxes to stoichiometric flame due to their lower burning velocity and least heat losses to the burner.
- (iv) The burning velocity is an important intrinsic factor influencing the heat transfer from laminar premixed flame impingements situations. Therefore, the exit gas velocity from the burner relative to the flame speed is an important parameter.
- (v) In comparison to flat plate, cylindrical surfaces have higher stagnation point heat fluxes.

In total an experimental dataset is generated which may be used for the improvement and validation of 1D flame models including heat transfer.

## Acknowledgments

The authors would like to thank Mr Stephan Steinbrink, and Dipl.-Ing. Andreas Görnt for their technical assistance in the setup build up, and much appreciation to Mrs Franziska Maculewicz, Faculty of Engineering and Center for Nano Integration (CENIDE) for the thermal conductivity measurements.

Financial support from the German Academic Exchange Service (DAAD) is gratefully acknowledged.

## ORCID iDs

Peter Obara Oketch  <https://orcid.org/0000-0001-6487-2017>

## References

- [1] Dong L L, Cheung C S and Leung C W 2001 Heat transfer characteristics of an impinging butane/air flame jet of low Reynolds number *Exp. Heat Transfer* **14** 265–82
- [2] Hofmann H M, Kind M and Martin H 2007 Measurements on steady state heat transfer and flow structure and new correlations for heat and mass transfer in submerged impinging jets *Int. J. Heat Mass Transfer* **50** 3957–65
- [3] Viskanta R 1993 Heat transfer to impinging isothermal gas and flame jets *Exp. Therm. Fluid Sci.* **6** 111–34
- [4] Morad M R, Momeni A, Ebrahimi Fordoei E and Ashjaee M 2016 Experimental and numerical study on heat transfer characteristics for methane/air flame impinging on a flat surface *Int. J. Therm. Sci.* **110** 229–40
- [5] Baukal C E 2013 *Oxygen-Enhanced Combustion* 2nd edn (Boca Raton, FL: CRC Press) pp 261–98
- [6] Chander S and Ray A 2007 Heat transfer characteristics of laminar methane/air flame impinging normal to a cylindrical surface *Exp. Therm. Fluid Sci.* **32** 707–21
- [7] Salem M, Staude S, Bergmann U and Atakan B 2010 Heat flux measurements in stagnation point methane/air flames with thermographic phosphors *Exp. Fluids* **49** 797–807
- [8] Allison S W and Gillies G T 1997 Remote thermometry with thermographic phosphors: Instrumentation and applications *Rev. Sci. Instrum.* **68** 2615–50
- [9] Brübach J, van Veen E and Dreizler A 2008 Combined phosphor and CARS thermometry at the wall–gas interface of impinging flame and jet systems *Exp. Fluids* **44** 897–904
- [10] Fuhrmann N, Schild M, Bensing D, Kaiser S A, Schulz C, Brübach J and Dreizler A 2012 Two-dimensional cycle-resolved exhaust valve temperature measurements in an optically accessible internal combustion engine using thermographic phosphors *Appl. Phys. B* **106** 945–51
- [11] Euler M, Zhou R, Hochgreb S and Dreizler A 2014 Temperature measurements of the bluff body surface of a swirl burner using phosphor thermometry *Combust. Flame* **161** 2842–8
- [12] Mohammed M A 2014 Experimental investigation of the heat flux from laminar premixed ethanol/air and hydrogen/ethanol/air flames to walls using thermographic phosphors *PhD Thesis* University of Duisburg-Essen URN (NBN) <https://urn:nbn:de:hbz:464-20150213-111206-3>
- [13] Seat H C and Sharp J H 2004 Dedicated temperature sensing with C-axis oriented single-crystal ruby ( $\text{Cr}^{3+}:\text{Al}_2\text{O}_3$ ) fibers: temperature and strain dependences of R-line fluorescence *IEEE Trans. Instrum. Meas.* **53** 140–54
- [14] Fuhrmann N, Baum E, Brübach J and Dreizler A 2011 High-speed phosphor thermometry *Rev. Sci. Instrum.* **82** 104903
- [15] Ek S, Anderson B and Svanberg S 2008 Compact fiber-optic fluorosensor employing light-emitting ultraviolet diodes as excitation sources *Spectrochim. Acta B* **63** 349–53
- [16] Pflitsch C, Vieffhaus D and Atakan B 2007 CVD of thin ruby films on Si(100) and stainless steel for surface temperature sensor applications *Chem. Vap. Depos.* **13** 420–6
- [17] Allison S W, Cates M R and Gillies G T 2002 Excitation of thermographic phosphors using a blue light emitting diode: spectral characteristics and instrumentation applications *Rev. Sci. Instrum.* **73** 1832–4
- [18] Atakan B, Eckert C and Pflitsch C 2009 Light emitting diode excitation of  $\text{Cr}^{3+}:\text{Al}_2\text{O}_3$  as thermographic phosphor: experiments and measurement strategy *Meas. Sci. Technol.* **20** 75304
- [19] Dragomirov P, Mendieta A, Abram C, Fond B and Beyrau F 2018 Planar measurements of spray-induced wall cooling using phosphor thermometry *Exp. Fluids* **59** 568
- [20] Fuhrmann N, Brübach J and Dreizler A 2013 Phosphor thermometry: a comparison of the luminescence lifetime and the intensity ratio approach *Proc. Combust. Inst.* **34** 3611–8
- [21] Yousefi-Asli V, Houshfar E, Beygi-Khosroshahi F and Ashjaee M 2018 Experimental investigation on temperature field and heat transfer distribution of a slot burner methane/air flame impinging on a curved surface *Appl. Therm. Eng.* **129** 761–71
- [22] Korobeinichev O, Gonchikzhapov M, Tereshchenko A, Gerasimov I, Shmakov A, Paletsky A and Karpov A 2018 An experimental study of horizontal flame spread over PMMA surface in still air *Combust. Flame* **188** 388–98
- [23] Skovorodko P A, Tereshchenko A G, Knyazkov D A, Paletsky A A and Korobeinichev O P 2012 Experimental and numerical study of thermocouple-induced perturbations of the methane flame structure *Combust. Flame* **159** 1009–15
- [24] Pflitsch C, Siddiqui R A and Atakan B 2008 Phosphorescence properties of sol–gel derived ruby measured as functions of temperature and  $\text{Cr}^{3+}$  content *Appl. Phys. A* **90** 527–32
- [25] Brübach J, Janicka J and Dreizler A 2009 An algorithm for the characterisation of multi-exponential decay curves *Opt. Lasers Eng.* **47** 75–9
- [26] Kaskan W E 1957 The dependence of flame temperature on mass burning velocity *Int. Symp. on Combustion* vol 6 pp 134–43
- [27] Chi T-C, Zhai G, Kook S, Chan Q N and Hawkes E R 2019 Application of LED-based thermographic phosphorescent technique to diesel combustion chamber walls in a pre-burn-type optical constant-volume vessel *Exp. Fluids* **60** 19453
- [28] Knappe C, Algotsson M, Andersson P, Richter M, Tunér M, Johansson B and Aldén M 2013 Thickness dependent variations in surface phosphor thermometry during transient combustion in an HCCI engine *Combust. Flame* **160** 1466–75
- [29] Atakan B and Roskosch D 2013 Thermographic phosphor thermometry in transient combustion: a theoretical study of heat transfer and accuracy *Proc. Combust. Inst.* **34** 3603–10
- [30] Kline S J and McClinock F A 1953 Describing uncertainties in single sample experiments *Mech. Eng.* **75** 3–8 ([https://www.scirp.org/\(S\(i43dyn45teexjx455qlt3d2q\)\)/reference/ReferencesPapers.aspx?ReferenceID=850270](https://www.scirp.org/(S(i43dyn45teexjx455qlt3d2q))/reference/ReferencesPapers.aspx?ReferenceID=850270))
- [31] Bosschaart K J and de Goey L P H 2003 Detailed analysis of the heat flux method for measuring burning velocities *Combust. Flame* **132** 170–80
- [32] Pilgrim C C, Feist J P and Heyes A L 2013 On the effect of temperature gradients and coating translucence on the accuracy of phosphor thermometry *Meas. Sci. Technol.* **24** 105201
- [33] Dong L L, Cheung C S and Leung C W 2002 Heat transfer from an impinging premixed butane/air slot flame jet *Int. J. Heat Mass Transf.* **45** 979–92
- [34] Van der Meer T 1987 Heat transfer from impinging flame jets *PhD Thesis* Delft University of Technology (<https://>

- [repository.tudelft.nl/islandora/object/uuid:e4a6859e-4864-4d72-b98d-44a9ff5e28ef/datastream/OBJ/view](https://repository.tudelft.nl/islandora/object/uuid:e4a6859e-4864-4d72-b98d-44a9ff5e28ef/datastream/OBJ/view))
- [35] Wang X L, Motala D, Lu T J, Song S J and Kim T 2014 Heat transfer of a circular impinging jet on a circular cylinder in crossflow *Int. J. Therm.Sci.* **78** 1–8
- [36] Giralt F, Chia C J and Trass O 1977 Characterization of the impingement region in an axisymmetric turbulent jet *Ind. Eng. Chem. Fundamen.* **16** 21–8
- [37] Çengel Y A 1997 *Introduction to Thermodynamics and Heat Transfer* (New York, NY: McGraw-Hill) pp 513–25